communications chemistry

Article

https://doi.org/10.1038/s42004-024-01285-1

Resolving intermediates during the growth of aluminum deuteroxide (Hydroxide) polymorphs in high chemical potential solutions

Check for updates

Hsiu-Wen Wang [1] ✉, Emily T. Nienhuis[2], Trent R. Graham[2], Maxime Pouvreau [2], Jacob G. Reynolds[3], Mark Bowden [2], Gregory K. Schenter [2], James J. De Yoreo [2,4], Kevin M. Rosso [2] & Carolyn I. Pearce [2,5]

Aluminum hydroxide polymorphs are of widespread importance yet their kinetics of nucleation and growth remain beyond the reach of current models. Here we attempt to unveil the reaction processes underlying the polymorphs formation at high chemical potential. We examine their formation in-situ from supersaturated alkaline sodium aluminate solutions using deuteration and time-resolved neutron pair distribution function analyses, which indicate the formation of individual $Al(OD)_3$ layers as an intermediate particle phase. These layers ultimately stack to form gibbsite- or bayerite-like layered heterostructures. Ex-situ characterization of the recovered precipitates using ^{27}Al magic angle spinning nuclear magnetic resonance spectroscopy, Raman, X-ray diffraction, and scanning electron microscopy, suggests the presence of additional intermediate states, an amorphous compound bearing both tetrahededrally- and penta-coordinated Al^{3+}. These observations reveal the complex pathways to form $Al(OD)_3$ monolayers via either transient pentacoordinate species or amorphous-to-ordered transitions. The subsequent crystallization of admixed gibbsite/bayerite is followed by an $Al(OD)_3$ monolayer attachment process.

Mineral growth and dissolution are of widespread importance across natural systems and industry. However, predicting rates of these processes still often relies upon phenomenological models that are based on fits to macroscopic observables. Identifying the underlying mechanistic pathways is essential for making conceptual advances in system predictability. For nucleation and growth, this includes understanding aspects such as the formation of oligomeric precursors to nucleation, and the assembly of nanoparticles as building blocks during crystal growth[1–4]. Differentiating between classical and nonclassical nucleation, beyond the thermodynamic arguments, inevitably relies on molecular-level insights at the relevant timescale and the ability to resolve the structure and (meta)stability of critical nuclei or amorphous precursors during the reaction process[4–7]. However, capturing the intermediate and/or end states, some of which are kinetically controlled (e.g., intermediates need to exchange with ions in solution to move to the next stage) and some thermodynamically controlled (e.g., free energy barriers favor nucleation of intermediates when the chemical potential is high), at the atomic scale is challenging, even using state-of-the-art tools, e.g., refs. 3,8–11. The demanding signal-to-noise ratio (sensitivity), in practice, represents a persistent barrier to identifying signals from intermediate species, including candidate cluster growth units, which are often short-lived and may only possess short-range order (i.e., roughly 3–5 atomic shells), making them difficult to differentiate from matrix/background signals.

For example, reactions in highly concentrated sodium aluminate solutions (brines) are one of the important subjects of research in aluminum chemistry. These solutions are central to the Bayer process in the alumina industry[12,13], where alkaline sodium hydroxide solutions ($NaOH_{(aq)}$) are used for the selective extraction of aluminum from bauxite ores. Concentrated caustic alkaline aluminate solutions are also important for the retrieval and processing of radioactive waste at the Department of Energy's

[1]Chemical Sciences Division, Oak Ridge National Laboratory, Oak Ridge, TN, USA. [2]Pacific Northwest National Laboratory, Richland, WA, USA. [3]Washington River Protection Solutions, LLC, Richland, WA, USA. [4]Department of Materials Science and Engineering, University of Washington, Seattle, WA, USA. [5]Department of Crop and Soil Sciences, Washington State University, Pullman, WA, USA. ✉e-mail: wanghswen@gmail.com

legacy nuclear sites, e.g., Hanford[14,15], where chemical conditions must be tuned to stabilize the solutions and prevent precipitation in processing pipes[16,17]. The Na_2O-Al_2O_3-H_2O ternary system is studied here as a simple representation of radioactive waste solutions (minus other soluble oxyanion species, such as nitrate, nitrite, sulfate, carbonate, and phosphate), and in this ternary system, we have learned that the metastability, nucleation kinetics, and growth phase(s) can be controlled by varying the Na^+/Al^{3+} mole ratios[18].

The thermodynamically controlling Al^{3+}-bearing solid phases from alkaline sodium aluminate solutions are known, but the mechanism of Al^{3+} coordination change upon going from dissolved species to the solid phase is unknown. To date, only two forms of tetrahedrally-coordinated aluminate dissolved species have been identified, the $Al(OH)_4^-$ monomer and the μ_2-oxo $Al_2O(OH)_6^{2-}$ dimer[18–20]. The existence of higher-order oligomeric species remains difficult to confirm experimentally. At low [NaOH] (less than ~10 molality, m), these monomers and dimers are thus considered as active species responsible for coordination transformation from tetrahedral-Al^{3+} in solution to octahedral-Al^{3+} in precipitating solids during crystallization of aluminum hydroxide ($Al(OH)_3$:gibbsite or its structural polymorphs)[4,18]. When the Na^+/Al^{3+} mole ratios are greater than ~1 and the total [NaOH] is above ~10 m, the sodium aluminate salts, monosodium aluminate hydrate (MSA: $Na_2[Al_2O_3(OH)_2]\cdot 1.5H_2O$) or nonasodium aluminate hydrate (NSA: $Na_9[Al(OH)_6]_2(OH)_3\cdot 6H_2O$) are solubility-controlling phases[18,21]. The MSA structure is composed of tetrahedral aluminate sheets, each sharing three corners (as bridging μ_2-oxygens) and one unbridged hydroxy apex[22–24], forming an open two-dimensional structure, with the general formula of $[Al_2O_3(OH)_2]_n^{2n-}$. The open structure results in large interstitial sites between the sheets, which can be occupied by Na^+ and H_2O molecules. The NSA structure is built with isolated $Al(OH)_6^{3-}$ octahedral complexes that are linked together by the OH^-, Na^+ and H_2O molecules[22,25]. If specific aluminate complexes, comprising part or all elements of the solid structure, need to be in solution in order to facilitate nucleation reactions, they would be octahedral $Al(OH)_x(H_2O)_{6-x}^{(3-x)}$ species for $Al(OH)_3$ and NSA, and large negatively charged tetrahedral aluminate oligomers consisting of a high ratio of μ_2-oxygen sites for MSA. Unless these assumed complexes, or other potential transition states, such as penta-coordinate or amorphous aluminate compounds, can be characterized, our mechanistic understanding of crystallization of Al^{3+}-bearing solid phases from alkaline sodium aluminate solutions remains unclear.

Building upon our understanding of the structure and reactivity of alkaline aluminate solutions, and how these interactions influence the constituents and structures of precipitated aluminum hydroxy (an) hydrates[4,18], we targeted a specific concentration (in a deuterated form), where the solution is supersaturated with respect to aluminum deutroxide ($Al(OD)_3$) as the primary phase, and deuterated MSA as the secondary phase. Deuteration was chosen to enhance our ability to discern key precursor species using neutron total scattering methods. This deuterated/supersaturated sodium aluminate solution, with a composition of 9 m $[Al^{3+}]$ + 9.9 m $[Na^+]$ + 36.9 m $[OD^-]$ (in 55.51 mole of D_2O), contains ~70% monomers ($Al(OD)_4^-$) and ~30% dimers ($Al_2O(OD)_6^{2-}$), based on our previous study[18]. The timescale of each reaction step is important to identify the signature of key intermediates and the kinetics of the nucleation-crystallization reaction. Here, the composition was selected to match the requisite time resolution between a neutron experiment and the reaction kinetics with the initial intent to observe the transformation from tetrahedral-Al^{3+} in solution to octahedral-Al^{3+} in aluminum deutroxide crystals and/or to resolve intermediate states along the reaction processes. A similar experimental concept on matching the requisite time resolution to the reaction kinetics, for better signal-to-noise ratios, using synchrotron X-rays to resolve intermediate structural signatures during the aqueous reaction of Fe^{2+} and S^{2-} to the precipitation of FeS (mackinawite) was presented by Beauvais et al.[11]. Here, we aimed to follow the crystallization pathways of aluminum deutroxides from their solute state, using both in-situ and ex-situ approaches. This includes neutron total scattering and complementary ^{27}Al magic angle spinning nuclear magnetic resonance (MAS NMR) spectroscopy for in-situ homogeneous nucleation measurements, and a combination of ^{27}Al MAS NMR, Raman, X-ray diffraction (XRD), and scanning electron microscopy (SEM) imaging for ex-situ characterization of recovered precipitating solids. The goal of our study was to fill several gaps in the understanding of: (i) the nucleation pathways that lead to the formation of edge-sharing $Al(OD)_6$ octahedral monolayers during the initial stages of precipitation, (ii) the layer stacking and deuterium-bond (D-bond) cross-linkage between layers, necessary for the formation of $Al(OD)_3$ polymorphs (e.g., gibbsite vs. bayerite), and (iii) the role of the counterions (Na^+ in this case) and to what extent amorphous compounds, composed of predominantly tetrahedral aluminate species, impede nucleation and growth mechanisms.

Results and discussion

In-situ observation of homogeneous nucleation and growth

To characterize the intermediate states leading to the formation of aluminum deutroxides, the aqueous reaction of NaOD-aluminate was studied in situ using neutron total scattering and pair distribution function (PDF) analysis. The PDF G(r) data, obtained from Fourier transformation of the collected/normalized scattering structure factor S(q), provides a localized view on the probability of finding pairs of atoms separated by some distance, r. The method is thus well suited to understand nanoscale and disordered phases, and if the data requisite times match the reaction kinetics, time-resolved PDF analysis can provide insight into structural evolution, such as nucleation and growth events. Figure S1 (in Supplementary Information, SI) displays infrared camera images captured during the neutron total scattering experiments over a period of 36 h, starting from a homogenous solution to the formation of precipitates. The images reveal a slow nucleation and growth reaction, where cloudiness appears during the first 16 h, then the precipitates begin to fall to the bottom of the tube during the subsequent 16–36 h. To capture structural signals from transient solution phase species, and reduce coherent diffraction signals from crystalline products, the neutron hot-zone was focused on the solution phase, and not the precipitates at the bottom of the tube (Fig. S1). The measured scattering structure factor S(q), corresponding to these infrared images, is given in Fig. S2a, emphasizing small intensity changes (~1–2%) and the practical sensitivity issues underlying in-situ total scattering experiments for probing nucleation and growth reactions. Other studies that probe such small intensity changes in total scattering can be found in refs. 11,26–28.

The $\Delta S(q)$ datasets were created by subtracting the first 4 h of collected data (as homogeneous solution signals) from each of the following time datasets (Fig. 1a). As seen in Fig. 1a, the $\Delta S(q)$ datasets indicate the formation of nanoscale solids over time, with Bragg reflections in the position agreeing with those expected for $Al(OD)_3$ polymorphs, including gibbsite, bayerite, doyleite and/or nordstrandite (in the sequence of decreasing thermodynamic stability[29,30]). These four polymorphs share the same layer structure, consisting of edge-sharing $Al(OD)_6$ octahedra forming an $Al(OD)_3$ dioctahedral layer. They differ from one another by the intralayer H/D-bonding orientations and the interlayer shift vectors, which together lead to variations in the geometry and strength of interlayer H/D-bonding (see their structures in Fig. S3). The intensity profile for the endpoint of the experiment (black curve in Fig. 1a) shows non-uniform peak broadening features, where the 4.32 $Å^{-1}$ reflection is noticeably narrower than the observed reflections at q values of ~3.63, ~3.83, ~4.72, and ~5.21 $Å^{-1}$. The 4.32 $Å^{-1}$ peak is mainly the 330 reflection of gibbsite, bayerite or nordstrandite, or the $30\bar{3}$ reflection of doyleite. Within the space group of gibbsite[31], bayerite[32] and nordstrandite[29], each $Al(OD)_3$ layer lies in the ab-plane and the layer stacking direction is along the c-axis. In the structure of doyleite[29], the layer is in the ac-plane and the stacking direction is along the b-axis (Fig. S3). Therefore, based on the layer stacking directions in each of the structures, the sharpness of the 4.32 $Å^{-1}$ peak is related to the mean crystallite dimension of the layers. Other peaks, including the main reflections near 2–3.4 $Å^{-1}$, are composed of mixed hkl indices, and thus the extent of broadening varies depending on the Miller index-l (in gibbsite, bayerite and nordstrandite) or -k (in doyleite) components. Commonly, non-

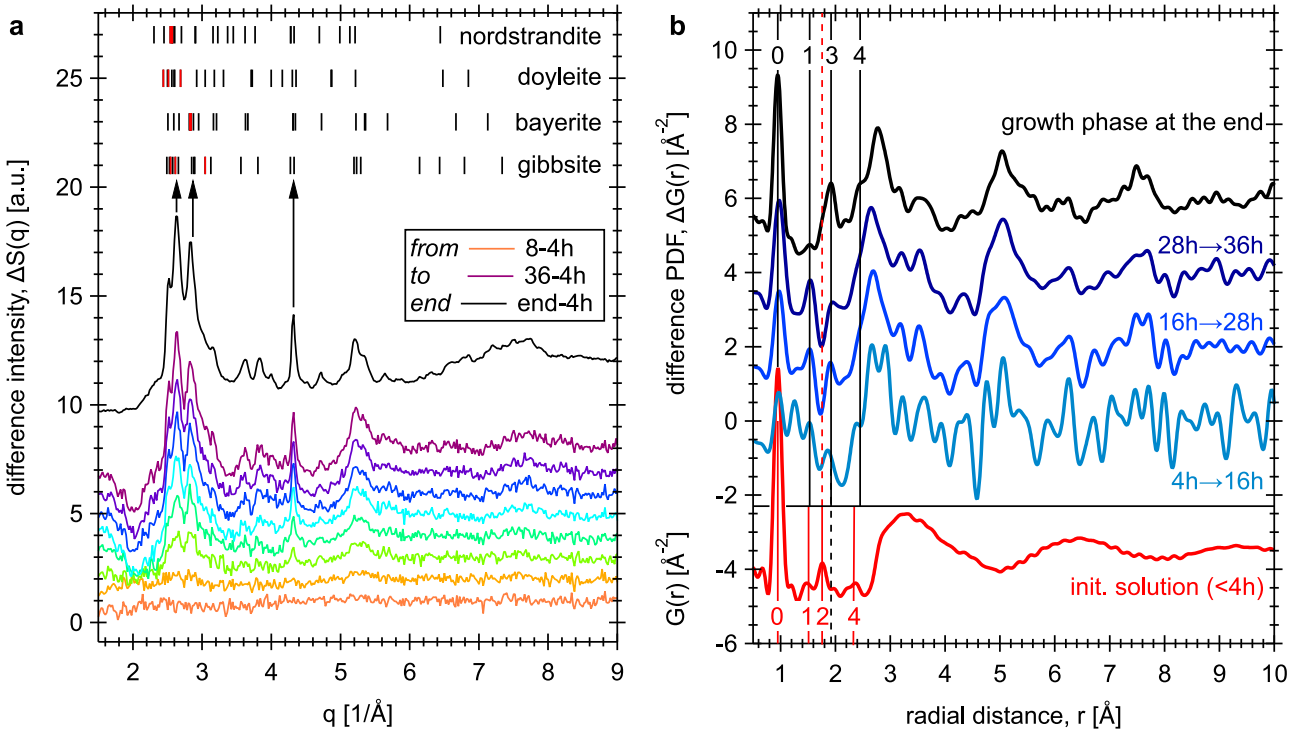

Fig. 1 | In-situ observation of nucleation and growth events using neutron total scattering. a Difference $\Delta S(q)$ curves every 4 h relative to the first 4 h dataset, showing the reaction progression as indicated by increasing peak intensities. The short ticks at the top of the plot indicate the expected neutron Bragg reflections (of the top 25 peak intensities) for the four $Al(OD)_3$ polymorphs. In each phase, the three most intense reflections are highlighted by red short ticks. These Bragg reflections are calculated using crystal structure data of Balan et al.[31] for gibbsite, Zigan et al.[32] for bayerite, and Demichelis et al.[29] for doyleite and nordstrandite. **b** Averaged difference PDF $\Delta G(r)$ datasets (blues and black curves) obtained at four different time intervals. The PDF of the initial solution structure (completed at/within 4 h after the solution was made) is shown by the red curve in the bottom panel. The vertical black and red lines indicate the relationship of PDF peaks between datasets (see texts for details). See also Fig. S2b, c for plots with extended q and r ranges, respectively.

uniform peak broadening in powder diffraction data is an indicative of anisotropic crystallite (or domain) size/strain line broadening[33]. For example, anisotropic crystallite size can result from crystal growth, where specific bonding interactions produce layered or columnar structures. Atomic dislocation-induced strain in comparison is a typical example of anisotropic strain broadening in a crystal[34]. Here, only the 4.32 $Å^{-1}$ reflection is noticeably narrower than other reflections, and its Miller index nicely matches to the expected intralayer lattice plane in the four $Al(OD)_3$ polymorphs. Thus, the observed non-uniform peak broadening and dependency on Miller indices for the 4.32 $Å^{-1}$ reflection suggest the lack of translational order along the stacking direction[33,35,36], e.g., random or turbostratic stacking, or finite-sized nanoparticles with anisotropic dimensions[37–39], e.g., suspended monolayers.

The difference PDF $\Delta G(r)$ were obtained via Fourier transformation of the $\Delta S(q)$ intensities (using q_{max} of 28 $Å^{-1}$) into the real-space signal (Fig. 1b). To reduce Fourier truncation ripples, a Lorch modification function was applied to each $\Delta S(q)$ to smooth derived $\Delta G(r)$ data. To improve signal-to-noise ratio, $\Delta G(r)$ datasets in time windows between 4–16, 16–28, and 28–36 h were then averaged, resulting in an 8–12 h interval for three $\Delta G(r)$ segments (Fig. 1b). These intermediate $\Delta G(r)$ curves show similar features to the signals obtained at the endpoint of the experiment, with overall intensities increasing with reaction time. In the initial solution PDF data (red curve in Fig. 1b), our previous geometric modeling[18] indicates that: (i) peak-0 at ~0.97 Å is the intramolecular O-D bonds in D_2O, OD^- and aluminate ions, (ii) peak-1 at ~1.51 Å is mostly the intramolecular D-D distances of a D_2O molecule, and (iii) peak-2 and -4 at ~1.79 and ~2.2–2.5 Å, respectively, correspond mainly to the intramolecular Al-O bonds and Al-D distances in tetrahedrally-coordinated aluminate species. These four peaks, and the aluminate-water and water-water correlations at longer distances, represent the initial solution structure, and are removed by the difference analysis. Therefore, the observed difference PDF $\Delta G(r)$ curves (top panel of Fig. 1b) represent the residual signals that contain pair-wise correlations involving primarily nucleating species, and their transformation into crystalline products.

To interpret the structure of the growth phase, a single two-dimensional $Al(OD)_3$ layer model was developed and tested to fit the PDF data observed at the endpoint of the experiment (Fig. 2a). This model consists of an isolated $Al(OD)_3$ layer created from the gibbsite structure[31], and no interlayer atom-atom correlations within the r-range being modeled (up to 30 Å; details are given in Section 1 of SI). Based on fitting results, peak intensities labeled 0, 3 and 4 (black) for the four sets of $\Delta G(r)$ data (Fig. 1b) correspond to the first coordination shell of O-D (~0.97 Å), Al-O (~1.91 Å), and Al-D (~2.3–2.5 Å) distances in an $Al(OD)_6$ octahedron. The relatively broad peaks/oscillations centered at ~2.7, ~5.0 and ~7.5 Å mainly reflect the ordered O-O + O-D distances in the $Al(OD)_3$ dioctahedral layer (e.g., in the dioctahedral layer the hexagonal cavities are patterned ~5 Å apart; see the insert structure in Fig. 2a). Note that peak-3 (Fig. 1b) also contains the intralayer D-bonds (~2–2.3 Å), which lie approximately in the *ab*-plane and point towards the vacant sites (Fig. 2a; insert structure). Accordingly, the growth reaction can be expressed as simply: $0.54Al(OD)_4^- + 0.23Al_2O(OD)_6^{2-} + 1.1Na^+ + 0.1OD^- + 0.23D_2O \rightarrow xAl(OD)_{3(s)} + (1\text{-}x)Al(OD)_4^- + 1.1Na^+ + (0.1+x)OD^-$, where the variable x defines the amount of precipitates (see the experimental section for solution composition). The intensity variations for the peak at ~1.53 Å (black peak-1 in Fig. 1b) do not match the $Al(OD)_3$ layer structural correlations. Considering that neutron PDF is sensitive to changes involving D-bearing species, this peak likely corresponds to D-bonding interactions between the deuteroxide-O_d and water-D_w sites (i.e., OD^- solvation correlations[18]), due to the change in solution composition upon precipitation. Alternatively, the ~1.53 Å peak could correspond to inner-sphere sorption of Na^+ to the

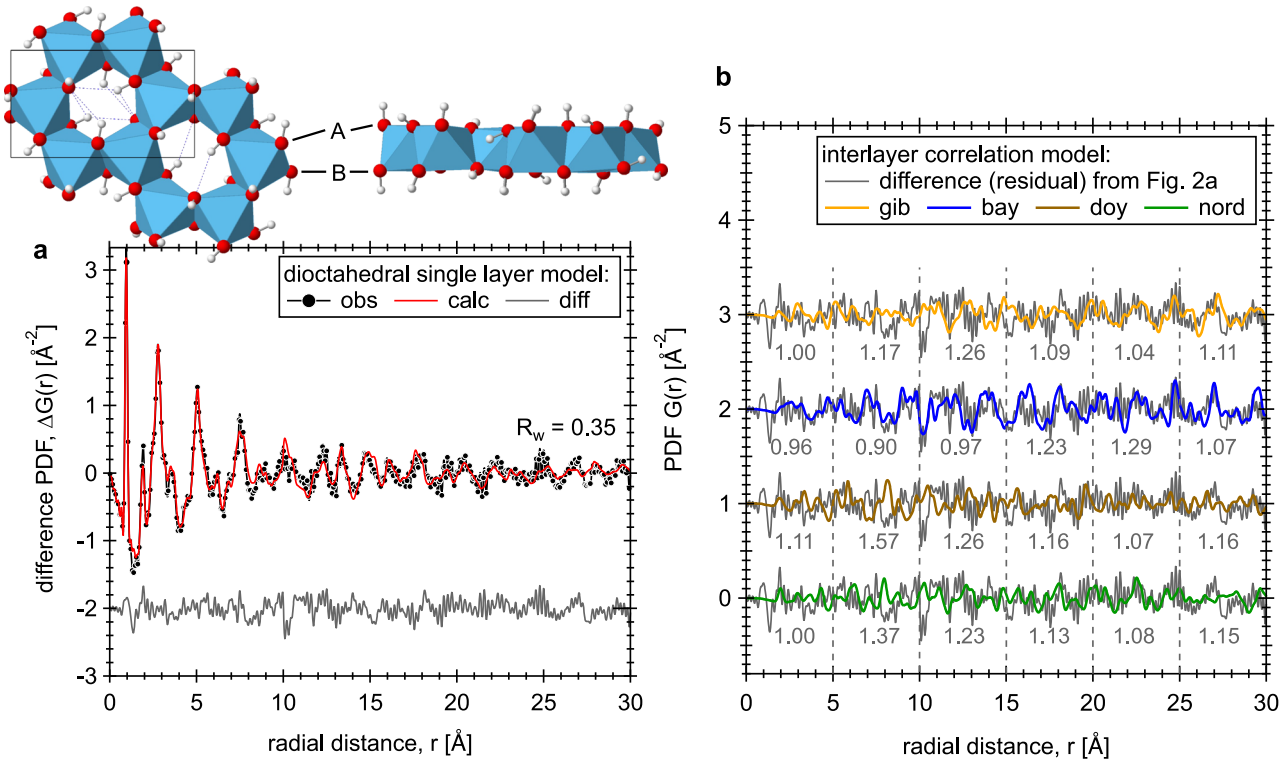

Fig. 2 | 2D Al(OD)$_3$ single layer model fit and comparison of the residual with four interlayer correlation models. a The black circles and the red curve show the observed and calculated PDFs, respectively, and the gray curve at the bottom shows the difference (residual) between the two (R_w = 0.35). The observed PDF data is obtained at the end of neutron experiment. The inset structural plot illustrates the top and side views of an Al(OD)$_3$ single layer. O atoms are shown as red spheres, D as white spheres, and Al as blue octahedra. The unit cell is outlined by black box, and intralayer D-bonds are shown as blue dashed lines. The A and B sites for the surface terminal-OD groups are also indicated. **b** The gray curve is the residual to the single layer model fit, and was repeated four times to facilitate comparison to the calculated interlayer correlations in all four types of Al(OD)$_3$ polymorphs. R_w values, calculated for every 5 Å segments of the residual data, are given at the bottom of the plot. See also Fig. S4 for the simulated neutron PDFs of Al(OD)$_3$ polymorphs. Here, crystal structure data of Balan et al.[31] for gibbsite, Zigan et al.[32] for bayerite, and Demichelis et al.[29] for doyleite and nordstrandite were used.

surface O-sites of the Al(OD)$_3$ layer, e.g., to the side of the hexagonal cavities, as predicted by molecular dynamics simulations of the gibbsite-NaOH$_{(aq)}$ interface[40]. The 4-to-16 h ΔG(r) data (light blue curve in Fig. 1b) also suggests a slightly shorter Al-O bonds than expected for Al-O bonds in octahedrally-coordinated configuration, i.e., the peak centered at 1.85 Å is in between the red dashed line (1.79 Å) for Al-O in tetrahedral aluminate species and the black solid line (1.91 Å) for Al-O in octahedral configuration. This intermediate Al-O bond length (between 1.79 and 1.91 Å) may indicate the presence of pentacoordinate species formed early in the reaction.

The residual from the fit of the single layer Al(OD)$_3$ model to the data (Fig. 2b) shows features that could correspond to: (i) solute ions and water molecules coordinated around the layer, and (ii) correlations associated with interlayer stacking. For (i), we expect the weak oscillating residual signal, restricted to the short r range (<10 Å), due to disordering of surface-bound water/ion species (see other examples in refs. 40–42). For (ii) on the evaluation of interlayer stacking, the residual data is compared with the calculated interlayer correlations (Fig. S4c; details are given in Section 2 of SI) for all four Al(OD)$_3$ polymorphs. As shown in Fig. 2b, on the basis of R_w analysis (in every 5 Å segments of the data), features in the residual curve correspond to the stacking patterns in either gibbsite or bayerite, but not to stacking patterns in nordstrandite and doyleite. Below ~15 Å, the residual curve corresponds to the bayerite stacking correlation, but between ~15–25 Å, the gibbsite stacking correlation model shows a better match to the overall oscillating widths and intensities (Fig. 2b). This indicates that individual Al(OD)$_3$ nanolayers are intermediary particles that stack together by oriented attachment to form gibbsite- or bayerite-like layered heterostructures.

Additional in-situ characterization using ^{27}Al MAS NMR was performed on a sodium aluminate solution of the same concentration (separately prepared) to follow the growth of gibbsite/bayerite phases over 2 weeks period. The ^{27}Al nucleus is quadrupolar, with a spin of 5/2, and the chemical shift of the resonance is sensitive to the Al^{3+} coordination environment. For Al^{3+}, the isotropic chemical shift is 0 to 20 ppm in octahedral coordination, 30 to 50 ppm in pentacoordination, and 60 to 80 ppm in tetrahedral coordination[43]. As shown in Fig. S6a, only a single Lorentzian line shape corresponding to tetrahedrally-coordinated aluminate species in solution can be observed initially. After ~3 days, signal intensity in the octahedral region starts to show, which displays a quasi-Lorentzian line attributing to the slow spinning rate. Under the performed acquisition conditions (see Section 3 of SI), individual resonances for bayerite-like or gibbsite-like nanolayers remain unresolved, and instead, a single octahedral resonance is observed, representing the combined octahedral coordination in both polymorphs. The relative integrated intensity of the octahedral Al^{3+} signal increases to about 3.5% in 2 weeks period (Fig. S6b). We note the variation in the induction time between the two in-situ measurements under the same solution concentration. If one considers the stochastic nature of nucleation and the formed nuclei have to grow to appreciable sizes before they can be detected experimentally, studies have shown that variation in the induction times determined from a large number of measurements under well-defined/identical conditions typically results an exponential distribution function[44,45]. Thus, ruling out concentration errors, variation in the induction times observed here may result from differences between neutron and NMR experiment conditions, such as temperature and solution volume used. Another possibility for such variation could originate from multiple nucleation and growth processes, i.e., not a single nucleation/growth

Table 1 | Results of XRD phase identification and Rietveld quantification (e.s.d. values in parentheses)

Sample	Phase abundance in wt%			
	Gibbsite	Bayerite	Amorphous[a]	MSA[b]
6 days – filtered	quantification is not performed[c]			--
45 days – filtered	42 (3)	22 (5)	35 (5)	--
3 months – filtered	40 (4)	25 (2)	35 (4)	--
3 months – D_2O washed	72 (4)	26 (4)	2 (3)	--
3 months – ETOD washed	35 (3)	3.8 (5)	48 (2)	13 (1)

[a]Amorphous phase fraction was quantified using 10 wt% TiO_2 (rutile) as an internal standard.
[b]MSA is monosodium aluminate hydrate.
[c]Due to the sample preparation errors (see Fig. S7), quantitative analysis for gibbsite, bayerite and amorphous phase content in the 6-days sample is subject to a great uncertainty and is not reported.

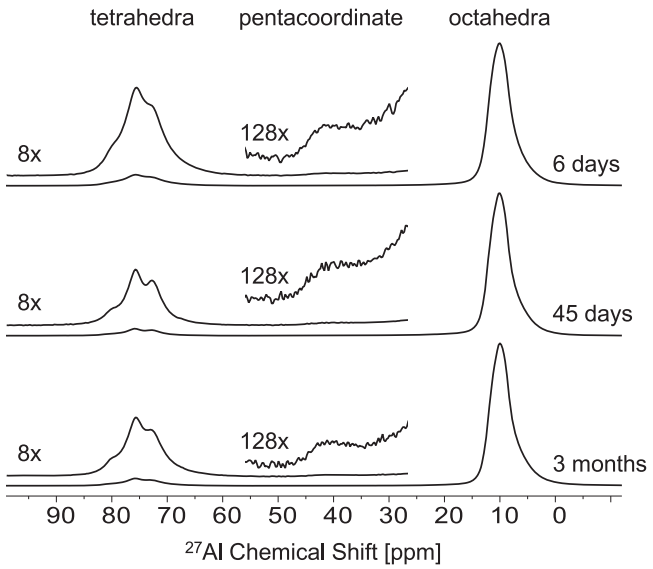

Fig. 3 | Ex-situ characterization of precipitates at three time points. Single pulse, direct excitation ^{27}Al MAS NMR spectra for precipitates collected/filtered after 6 days, 45 days, and 3 months. Vertical magnifications of select regions (8× in tetrahedra and 128× in pentacoordinate) are offset.

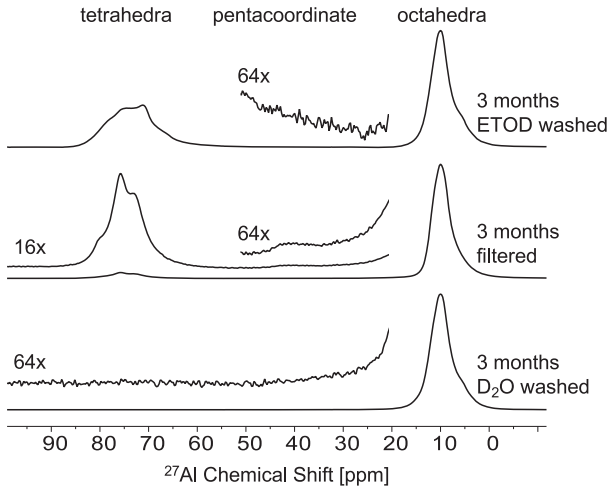

Fig. 4 | Effects of washing procedures on phase alternations. Single pulse, direct excitation ^{27}Al MAS NMR spectroscopy of precipitates after 3 months that were washed with D_2O, filtered only, or washed with ETOD. Vertical magnifications of select regions are offset. The filtered only sample is reproduced from Fig. 3 for comparison.

mechanism. That is during the initial stage of precipitation, the individual $Al(OD)_3$ layers could be formed by monomer-by-monomer addition to a candidate nucleus (classical nucleation), or they could grow from an amorphous phase that facilitates the coordination change of tetrahedral Al^{3+} to octahedral Al^{3+} (nonclassical nucleation). Ex-situ characterization of precipitates is performed to differentiate between these two potential pathways.

Ex-situ characterization of precipitates

Precipitates were retrieved, via vacuum filtration, from sodium aluminate solutions after the neutron experiment at three different time points: 6 days, 45 days, and 3 months. Based on a combination of XRD characterization and ^{27}Al MAS NMR spectroscopy, a clear signature of an amorphous phase was identified. The presence of an amorphous phase is expected, given the chemical complexity and high chemical potential of the starting solution. Quantitative phase analysis (Table 1) using the Rietveld method on XRD data showed that the precipitate is comprised of gibbsite and bayerite (consistent with in-situ neutron PDF analysis), and an amorphous phase (see XRD patterns in Figs. S7a, b and S8). The amount of gibbsite, bayerite and amorphous phase remained approximately constant across the time series. Raman spectra of the three precipitates also show band positions in the OD stretching vibration region corresponding to a mixture of gibbsite/bayerite (Fig. S9).

The coordination state of Al^{3+} in the amorphous phase was determined using solid-state^{27}Al MAS NMR. The ^{27}Al MAS NMR spectra (Fig. 3) indicate that Al^{3+} is present in tetrahedral, penta and octahedral coordinations over the course of the experiment. This is to our knowledge the first time that a pentacoordinated Al^{3+} signal has been resolved during nucleation and growth of gibbsite/bayerite from a supersaturated alkaline aluminate solution. Previously, pentacoordinated species have only been reported in amorphous aluminum hydroxides precipitated at near neutral pH, or in alumina produced from the calcination of aluminum hydroxide[46–48] and aluminum oxyhydroxide[49].

The precipitates retrieved via vacuum filtration were then washed with either deuterated water (D_2O) or deuterated ethanol (ETOD) at room temperature. ETOD was used to prevent dissolution of high soluble compounds, such as amorphous phases, during the washing step. The ^{27}Al MAS NMR spectrum of the precipitate washed with D_2O has only an octahedral resonance (Fig. 4) corresponding to gibbsite and/or bayerite, which is expected as these phases are poorly soluble in water (solubilities of $10^{-8.1}$ and $10^{-7.9}$ m[50,51], respectively, in pure water at 25 °C). The ^{27}Al MAS NMR spectrum for the precipitate washed with ETOD had both octahedral and tetrahedral resonances, suggesting that ETOD preserved the amorphous phase, which then partially crystallized into tetrahedral MSA, according to the XRD results (Table 1 and Fig. S7c). The pentacoordinated species was not observed in precipitates washed with either D_2O or ETOD. The wt% proportion of the phases was dependent on the washing process (Table 1), and different amounts of gibbsite and bayerite resulted in a subtle increase in the shoulder of the octahedral resonance near 5 ppm (Fig. 4).

To better resolve ^{27}Al resonances, ^{27}Al triple quantum MAS NMR (3QMAS NMR) spectroscopy was performed (Fig. 5). 3QMAS NMR spectroscopy reduces the second order quadrupolar broadening in MAS NMR spectra of quadrupolar nuclei by correlating multiple quantum coherences with their conversion into single quantum coherence[52]. This NMR acquisition results in two-dimensional spectra, where unique resonances that are often superimposed in one-dimensional spectra can be better resolved. However, the technique has low sensitivity compared to single pulse spectra (Figs. 3 and 4), so the less abundant pentacoordinated species is below the limit of detection in the 3QMAS NMR data. The ^{27}Al 3QMAS NMR spectra of the solids washed with ETOD exhibit at least two tetrahedral environments (Fig. 5e). The first resonance, at an F1 dimension

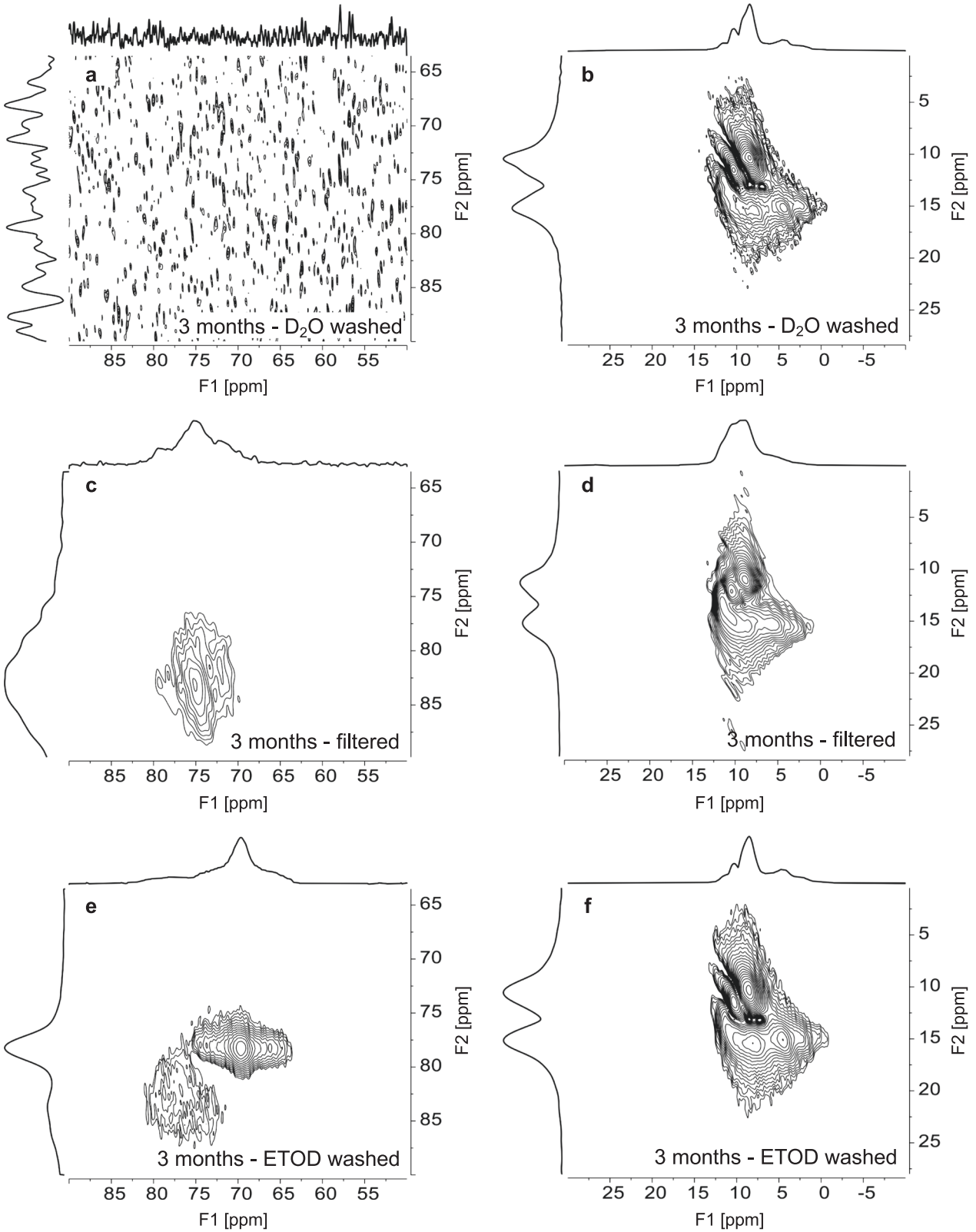

Fig. 5 | Verification of multiple Al^{3+} coordination states in precipitates. ^{27}Al 3QMAS NMR spectroscopy of samples washed with D_2O, filtered only, or washed with ETOD, respectively, at a field strength of 14.1 T. The tetrahedral region is shown in (**a**), (**c**), and (**e**). The octahedral region is shown in (**b**), (**d**), and (**f**).

of 69.7 and an F2 dimension of 78.3 ppm, exhibits a well-defined quadrupolar line shape and similar to the resonance for protonated MSA[22], in agreement with the XRD data. The second tetrahedral resonance is broad and shows no discernable quadrupolar line shape features, which can be attributed to tetrahedral aluminum in an amorphous phase. Only the second tetrahedral resonance corresponding to the amorphous phase is present in the spectrum for the filtered-only sample (Fig. 5c), and there are no tetrahedral resonances in the D_2O washed sample (Fig. 5a). In the octahedral region, the ^{27}Al 3QMAS NMR spectra shows three peaks (Figs. 5b, d, f). These can be assigned to the two Al sites in gibbsite and the

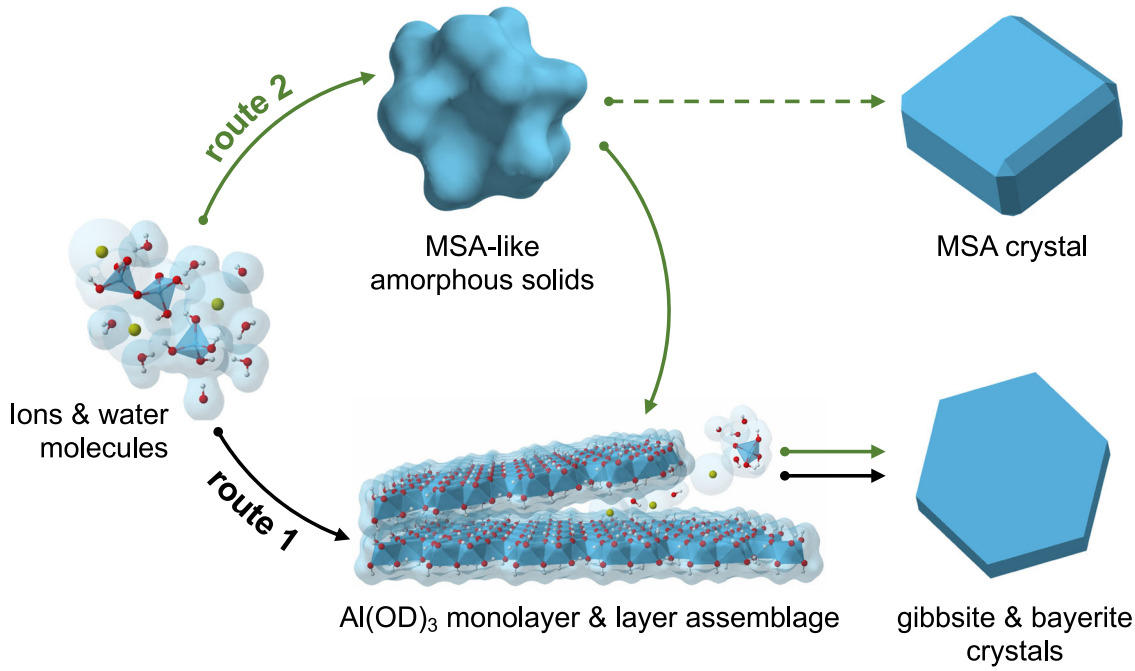

Fig. 6 | Schematic of multiple nucleation and growth processes. Gibbsite/bayerite formation from alkaline sodium aluminate solutions. The final faceted crystals are illustrative representations of final bulk crystal states. The exact crystal morphologies (SEM images in Fig. S10) are more complicated than the illustrations presented here.

two Al sites in bayerite, with partial overlap resulting in three peaks[43]. While the differences in wt. % of gibbsite and bayerite observed in XRD may be attributed to some changes in the octahedral region of the 3QMAS NMR spectra between the filtered and samples washed with ETOD or D_2O, these could also potentially mask subtle contributions of octahedrally-coordinated amorphous species.

The ex-situ NMR results indicate that transformation of Al^{3+} coordination from tetrahedral in solution to octahedral in aluminum deuteroxide may proceed either through, or in the presence of, an amorphous phase. This amorphous phase found in the current studied solutions is distinguished from other amorphous phases produced from neutralizing aqueous, acidic solutions of aluminum nitrate[53]. The amorphous phase is very sensitive to washing procedures, which may induce crystallization into gibbsite, bayerite, or monosodium aluminate hydrate (MSA). SEM images (Fig. S10), showing the morphology of aggregated solids, support XRD (Table 1) and NMR (Figs. 3–5) data. Washing with D_2O precipitates show platelet aggregates resembling typical gibbsite morphology[53,54], while precipitates washed with ETOD form smoother, more globular aggregates resembling an amorphous phase (Fig. S10). Note that there might have some potential impacts on products morphology with D[54], the exact isotope effects of D for H on the morphology and rates of precipitation are however beyond the scope of this work.

Multiple nucleation and growth processes

Combining both in-situ and ex-situ observations, Fig. 6 illustrates the proposed multiple reaction pathways for gibbsite/bayerite nucleation and growth from alkaline sodium aluminate solutions. The starting supersaturated solution contains a distribution of aluminate species featuring tetrahedral Al^{3+} coordination, i.e., monomers, dimers, and possibly larger oligomers, all of which can play a role in nucleation and growth. In route 1, the formation of $Al(OD)_3$ monolayers may start by monomer-by-monomer addition to form octahedrally-coordinated Al^{3+} nuclei, followed by the development of these nuclei into individual nanolayers visible to the naked eye (Fig. 6). This process is a classical nucleation and growth pathway in which the Al^{3+} coordination changed from tetrahedral in small aluminate species to octahedral in nanoplatelets is endergonic. The pentacoordinate Al^{3+} species found with solid state NMR spectroscopy, potentially bridges Al^{3+} coordination changes from tetrahedral solution species to octahedral Al^{3+} nuclei and/or is present at the edge of the nuclei. However, its presence is poorly abundant and not clearly resolvable via both the in-situ neutron total scattering and NMR approaches. At this stage of the reaction, the development of $Al(OD)_3$ monolayers, instead of direct growth of gibbsite/bayerite nanocrystals, are preferred likely due to the effects of: (i) the bond-valence sum requirements[55] between OD^- and octahedrally-coordinated Al^{3+} (i.e., 0.5 bond valences for each OD^- group in bridging two octahedrally coordinate Al^{3+}, forming a neutral charged $Al(OD)_3$ layer), and (ii) the stabilization of layers by interaction with surrounding water molecules, Na^+, and/or OD^-, which together act as steric forces preventing direct D-bonding between layers[40]. With time, the crystalline $Al(OD)_3$ monolayer intermediates ultimately assemble into gibbsite/bayerite structures by particle attachment and alignment processes.

The amorphous precipitates observed via ex-situ characterization suggest the presence of an alternative nonclassical pathway to gibbsite/bayerite crystallization (Fig. 6, route 2), via aggregation of Na^+-aluminate oligomeric precursors. This amorphous compound consists mainly tetrahedral Al^{3+} bridged together by μ_2-oxygene (i.e., similar to both the $Al_2O(OH)_6^{2-}$ dimer and the MSA phase), and with some minor pentacoordinated Al^{3+}. Association of pentacoordinate Al^{3+} species with the amorphous surface or as a part of oligomeric network formers would potentially provide a lower energy pathway enhancing Al^{3+} coordination transformation (from tetrahedra to octahedra) and growth of the $Al(OD)_3$ monolayers. Once the monolayers are formed, the subsequent layer assemblages can be expected, i.e., the processes likely similar to the fabrication of multilayer assemblies based on D/H bonding using the existing surfaces/seedings[56].

Alternatively, the two nucleation pathways leading to the formation of $Al(OD)_3$ monolayers, could be independent events. That is, the amorphous phases may not contribute substantially to the $Al(OD)_3$ layer nucleation and growth. The fact that we are able to observe amorphous materials from the precipitates after several months of dispersion in the solution suggests that the oligomeric precursors for the nucleation of amorphous intermediates may impede $Al(OD)_3$ layer formation via consuming active aluminate monomers/dimers species to form complex Na^+-aluminate-D_2O networks. This creates a dynamically arrested state for part of aluminate species within the amorphous network, where aluminate species may become active again

upon dissolution of amorphous precipitates. Particularly, if the free energy barriers to form gibbsite/bayerite from amorphous phase are too high to overcome, this would entail that the amorphous phase would eventually transfer only to the MSA salt (due to structure similarity) given a long reaction time or upon partial dehydration (Fig. 6; green dashed line).

The precipitation of $Al(OD)_3$ polymorphs (gibbsite vs. bayerite) from supersaturated alkaline aluminate solutions must also be addressed. In the past, using solubility data to reflect metastable equilibria[50,51,57], the tendency for bayerite formation (with respective to gibbsite) is generally understood as a result of metastable precipitate from supersaturated solutions. However, many of the thermodynamic properties of $Al(OD/H)_3$ polymorphs are controlled by modes of stacking of the $Al(OD/H)_3$ layers[29,30]. Thus, layer-by-layer assembly of $Al(OD)_3$ monolayers must play a significant role in polymorphism and phase selection. In the $Al(OD)_3$ monolayers, the surface -OD groups are in hexagonal close packing arrangements, and therefore the -OD groups are positioned differently on each side of the surfaces, termed A vs. B sites (Fig. 2a; top insert). In the processes of layer attachment, the likelihood of A-site termination seeing another A-site termination (A-A, or equivalently B-B) is the same as A-site termination seeing B-site termination (A-B or B-A). Hence, from a statistical point of view, the A-B stacking sequences (in bayerite, doyleite and nordstrandite) have the same occurrence probability as the A-A stacking sequences (in gibbsite). The lack of doyleite and nordstrandite phases indicates that the controlling reactions at the interfaces between two monolayers are complicated, involving not only the dynamics of water and ions in the interfacial region, but also the orientational movements of the terminal -OD groups, and their D-bond cross-linkage strength upon attachment. Our findings on gibbsite/bayerite-like layered heterostructures may provide insights into the development of mechanistic descriptions for layer assembly processes. A few of theoretical works dedicated to connect molecular-scale details and energy barriers for layer-layer interactions in aluminum (oxy)hydroxide systems can be found in refs. 58–63.

Conclusions

Although our mechanistic understanding of gibbsite (the stable thermodynamic phase) nucleation and growth pathways from the supersaturated sodium alkaline solution remains inconclusive, we have shown evidence that the precipitation is not a simple reaction involving the direct growth of ordered gibbsite somatoids from supersaturated solutions. Instead, it is accompanied by formation of bayerite and amorphous metastable phases. Key intermediate states, including pentacoordinate Al^{3+} species, $Al(OD)_3$ monolayers, and amorphous species, highlight a complex interplay of classical and nonclassical models of nucleation and growth. Cryogenic transmission electron microscopy to isolate layer formation and assemblage processes, and theoretical simulations using our newly developed reactive force field[64] and a semiempirical model[20] to study aluminate oligomerization and transition between different coordination states, are underway to provide a complete understanding of nucleation and growth processes at the molecular level.

Methods

Solution preparation

Deuterated sodium aluminate solution was generated by quantitative dissolution of degreased Al wire (99.999% grade) in 40 wt% stock NaOD solutions (in D_2O; Sigma-Aldrich, 372072, 99.5 atom % D), with selective D_2O water (Cambridge Isotope Laboratories, inc., DLM-6-S-50, 99.96 atom % D) addition or removal (by evaporation at elevated temperatures) as needed to achieve the desired concentration of 9 m $[Al^{3+}]$ + 9.9 m $[Na^+]$ + 36.9 m $[OD^-]$ (in 55.51 moles of D_2O). Here, concentration units are listed as molality (m), moles of solute per 55.51 moles of solvent (i.e., 1.11 kg of D_2O). This solution is exactly the same solution studied in our previous work (termed s0.1)[18]. Its composition corresponds roughly to speciation of 4.8 m $[Al(OD)_4^-]$ + 2.1 m $[Al_2O(OD)_6^{2-}]$ + 9.9 m $[Na^+]$ + 0.9 m $[OD^-_{excess}]$, where the monomeric $Al(OD)_4^-$ and the dimeric $Al_2O(OD)_6^{2-}$ solution species have relative abundance of ~70% and ~30%, respectively, according to our previous Raman study[18]. The $[OD^-_{excess}]$ represents the excess amount of OD^- species that is not consumed by $Al(OD)_4^-$ and $Al_2O(OD)_6^{2-}$ formation. Thus, the solution has stoichiometric expression of $0.54Al(OD)_4^- + 0.23Al_2O(OD)_6^{2-} + 1.1Na^+ + 0.1OD^-_{excess}$. During the preparation, an ultra-high purity, Ar-filled glovebox were used to protect solution against CO_2 capture known to be significant for concentrated NaOD solutions at ambient conditions and to prevent isotope exchange of H_2O for D_2O and OH^- for OD^- that can occur upon exposure to ambient atmospheric conditions.

Neutron total scattering measurement

Neutron total scattering data was collected at the NOMAD beamline at the Spallation Neutron Source, Oak Ridge National Laboratory[65]. A thin-walled vessel, incorporating commercially-available 5 mm diameter Wilmad fused quartz NMR tubes and PTFE Swagelok seals, was used as the sample cell. Approximately 3 ml of solution was loaded into the sample cell in an Ar environment at ambient pressure, and was quickly transported to the beamline for neutron total scattering measurements. The sample vessel was mounted vertically in the NOMAD linear sample changer with an argon cryostream fixed below the aligned sample position. Scattering data were collected in 24 min frames at 290 K in an Argon atmosphere over the ~36 h duration of the experiment. Sequential groups of ten datasets were averaged prior further analysis, resulting in a 4 h data segment interval. The beamline's auto-reduction software[65] was used to normalize collected data, subtract background and container scattering signals, and produce histograms appropriate for PDF analysis. PDF patterns were calculated via Fourier transformation of the $S(q)$ data utilizing a q_{max} of 28 $Å^{-1}$ and a Lorch modification function was applied to smooth data.

Nuclear magnetic resonance spectroscopy

In-situ ^{27}Al MAS NMR spectra were acquired on an 11.7467 T NMR spectrometer using a 7.5 mm HX probe at ~20 °C and a spinning rate of 100 Hz. Ex-situ single-pulse direct excitation ^{27}Al MAS NMR spectra were obtained with a Bruker NMR spectrometer at a field strength of 14.1 T. ^{27}Al triple quantum MAS (3QMAS) NMR spectra were also acquired at a field strength 14.1 T using a 2.5 mm MAS probe with the z-filter, ^{27}Al 3QMAS pulse sequence (mp3qzqf). Please see Section 3 of the supporting text for details on acquisition parameters.

X-ray diffraction

Powder X-ray diffraction was performed on a Rigaku SmartLab SE diffractometer using Cu-Kα radiation (λ = 1.5418 Å) with generator settings of 44 mA and 40 keV. Data were obtained at a scan rate of 0.9 °2θ/min with a step size of 0.01° from 2–100 °2θ using a position-sensitive D/teX ultra-detector with 250 individual detection elements. To quantify an amorphous fraction, 10 wt% rutile (TiO_2 standard reference material #674) was added as a crystalline internal standard. To ensure homogenous distribution of the rutile standard and to minimize CO_2 adsorption, the sample and standard were mixed in an agate mortar and pestle in an N_2 glovebox, and samples were loaded into zero-background cavity holder. Rietveld refinement was performed using TOPAS Software (Bruker ASX). Details about sample preparation and X-ray Rietveld-internal standard refinements are given in Section 4 of the supporting text.

Raman spectroscopy

Raman spectroscopy was performed using a Horiba LabRam HR spectrometer with a Nikon Ti-E inverted microscope using a 632.81 nm continuous laser light source focused through a 40x microscope objective. Spectra were collected between a range of 100–4000 cm^{-1} with a resolution of 1 cm^{-1}. For each sample, ten spectra were collected with a 30 s exposure time and then averaged. Raman spectra were collected on the filtered supernatant of the original solution (following neutron experiment) and on the solution prepared for the time point study (prior/after precipitation).

Data availability

The article and Supplementary Information contain all the data necessary to support the study's findings and conclusions. Any relevant data, including

neutron/X-ray diffraction and Raman, are available from the authors upon reasonable request. Tabulated source data for ^{27}Al MAS NMR spectra in Figs. 3–5 and in Fig. S6a is provided in Supplementary Data 1.

Received: 1 March 2024; Accepted: 28 August 2024;
Published online: 04 September 2024

References

1. De Yoreo, J. J. et al. Crystallization by particle attachment in synthetic, biogenic, and geologic environments. *Science* **349**, aaa6760 (2015).
2. Rao, A. & Colfen, H. From solute, fluidic and particulate precursors to complex organizations of matter. *Chem. Rec.* **18**, 1203–1221 (2018).
3. Gebauer, D. & Wolf, S. E. Designing solid materials from their solute state: a shift in paradigms toward a holistic approach in functional materials chemistry. *J. Am. Chem. Soc.* **141**, 4490–4504 (2019).
4. Wang, H.-W., Yuan, K., Rampal, N. & Stack, A. G. Solution and interface structure and dynamics in geochemistry: gateway to link elementary processes to mineral nucleation and growth. *Cryst. Growth Des.* **22**, 853–870 (2021).
5. Sosso, G. C. et al. Crystal nucleation in liquids: open questions and future challenges in molecular dynamics simulations. *Chem. Rev.* **116**, 7078–7116 (2016).
6. Smeets, P. J. M. et al. A classical view on nonclassical nucleation. *Proc. Natl Acad. Sci. USA* **114**, E7882–E7890 (2017).
7. Xu, S., Zhang, H., Qiao, B. & Wang, Y. Review of liquid–liquid phase separation in crystallization: from fundamentals to application. *Cryst. Growth Des.* **21**, 7306–7325 (2021).
8. Gebauer, D. & Cölfen, H. Prenucleation clusters and non-classical nucleation. *Nano Today* **6**, 564–584 (2011).
9. Henzler, K. et al. Supersaturated calcium carbonate solutions are classical. *Sci. Adv.* **4**, eaao6283 (2018).
10. Fetisov, E. O. et al. Nanometer-scale correlations in aqueous salt solutions. *J. Phys. Chem. Lett.* **11**, 2598–2604 (2020).
11. Beauvais, M. L., Chupas, P. J., O'Nolan, D., Parise, J. B. & Chapman, K. W. Resolving single-layer nanosheets as short-lived intermediates in the solution synthesis of FeS. *ACS Mater. Lett.* **3**, 698–703 (2021).
12. Hind, A. R., Bhargava, S. K. & Grocott, S. C. The surface chemistry of Bayer process solids: a review. *Colloids Surf. A* **146**, 359–374 (1999).
13. Tabereaux, A. T. & Peterson, R. D. In *Treatise on Process Metallurgy* (ed. Seshadri Seetharaman) 839–917 (Elsevier, 2014).
14. Clark, S. B., Buchanan, M. & Wilmarth, B. *Basic research needs for environmental management* (Pacific Northwest National Lab, 2016).
15. Colburn, H. A. & Peterson, R. A. A history of Hanford tank waste, implications for waste treatment, and disposal. *Environ. Prog. Sustain.* **40**, e13567 (2020).
16. Reynolds, J. G. The apparent solubility of aluminum (III) in Hanford high-level waste. *J. Environ. Sci. Health A* **47**, 2213–2218 (2012).
17. Reynolds, J. G., McCoskey, J. K. & Herting, D. L. Gibbsite solubility in Hanford nuclear waste approached from above and below saturation. *Ind. Eng. Chem. Res.* **55**, 5465–5473 (2016).
18. Nienhuis, E. T. et al. Structure and reactivity of sodium aluminate complexes in alkaline solutions. *J. Mol. Liq.* **367**, 120379–120392 (2022).
19. Pouvreau, M. et al. Ab initio molecular dynamics reveal spectroscopic siblings and ion pairing as new challenges for elucidating pre-nucleation aluminum speciation. *J. Phys. Chem. B* **122**, 7394–7402 (2018).
20. Pouvreau, M. et al. Mechanisms of Al^{3+} dimerization in alkaline solutions. *Inorg. Chem.* **59**, 18181–18189 (2020).
21. Qiu, G. F. & Chen, N. Y. Phase study of the system Na_2O-Al_2O_3-H_2O. *Can. Metall. Q.* **36**, 111–114 (1997).
22. Graham, T. R. et al. Solid-state recrystallization pathways of sodium aluminate hydroxy hydrates. *Inorg. Chem.* **59**, 6857–6865 (2020).
23. Kaduk, J. A. & Pei, S. The crystal structure of hydrated sodium aluminate, $NaAlO_2{\cdot}5/4H_2O$, and its dehydration product. *J. Solid State Chem.* **115**, 126–139 (1995).
24. Grishchenko, R. O. & Emelina, A. L. Synthesis and thermochemical characteristics of $Na_2O{\cdot}Al_2O_3{\cdot}2.5H_2O$. *Russ. J. Phys. Chem. A* **87**, 1–5 (2012).
25. Weinberger, M., Schneider, M., Zabel, V., Müller, D. & Gessner, W. Nonanatrium-Bis (Hexahydroxoaluminat)-Trihydroxid-Hexahydrat ($Na_9[Al(OH)_6]_2(OH)_3{\cdot}6H_2O$) - Kristallstruktur, Nmr-Spektroskopie Und Thermisches Verhalten. *Z. Anorg. Allg. Chem.* **622**, 1799–1805 (1996).
26. Jensen, K. M. et al. Revealing the mechanisms behind SnO_2 nanoparticle formation and growth during hydrothermal synthesis: an in situ total scattering study. *J. Am. Chem. Soc.* **134**, 6785–6792 (2012).
27. Page, K., Stack, A. G., Chen, S. A. & Wang, H. W. Nanopore facilitated monohydrocalcitic amorphous calcium carbonate precipitation. *Phys. Chem. Chem. Phys.* **24**, 18340–18346 (2022).
28. Brady, A. B. et al. In situ observations of barium sulfate nucleation in nanopores. *Cryst. Growth Des.* **22**, 6941–6951 (2022).
29. Demichelis, R., Catti, M. & Dovesi, R. Structure and stability of the $Al(OH)_3$ polymorphs doyleite and nordstrandite: a quantum mechanical ab initio study with the CRYSTAL06 Code. *J. Phys. Chem. C* **113**, 6785–6791 (2009).
30. Demichelis, R., Civalleri, B., Noel, Y., Meyer, A. & Dovesi, R. Structure and stability of aluminium trihydroxides bayerite and gibbsite: a quantum mechanical ab initio study with the Crystal06 code. *Chem. Phys. Lett.* **465**, 220–225 (2008).
31. Balan, E., Lazzeri, M., Morin, G. & Mauri, F. First-principles study of the OH-stretching modes of gibbsite. *Am. Mineral.* **91**, 115–119 (2006).
32. Zigan, F., Joswig, W. & Burger, N. Die Wasserstoffpositionen im Bayerit, $Al(OH)_3$. *Z. Kristallogr. Cryst. Mater.* **148**, 255–274 (1978).
33. Madsen, I. C., Scarlett, N. V. Y., Kleeberg, R. & Knorr, K. In *International Tables for Crystallography* Vol. H. *Powder Diffraction* (eds. Gilmore, C. J., Kaduk, J. A. & Schenk, H.) Ch. 3.9, 344–373 (2019).
34. Černý, R. & Favre-Nicolin, V. In *International Tables for Crystallography* Vol. H. *Powder Diffraction* (eds. C. J. Gilmore, J. A. Kaduk & H. Schenk) Ch. 4.5, 442–451 (2019).
35. Treacy, M. M. J., Newsam, J. M. & Deem, M. W. A general recursion method for calculating diffracted intensities from crystals containing planar faults. *Proc. R. Soc. Lond. A* **433**, 499–520 (1997).
36. Ramesh, T. N., Jayashree, R. S. & Kamath, P. V. Disorder in layered hydroxides: diffax simulation of the x-ray powder diffraction patterns of Nickel Hydroxide. *Clays Clay Min.* **51**, 570–576 (2003).
37. Kumpf, C. Structure determination of very small (1–5 nm) nano-particles. *Appl. Phys. A* **85**, 337–343 (2006).
38. Zhang, X. et al. Boehmite and Gibbsite nanoplates for the synthesis of advanced alumina products. *ACS Appl. Nano Mater.* **1**, 7115–7128 (2018).
39. Leoni, M. In *International Tables for Crystallography* Vol. H. *Powder Diffraction* (eds. Gilmore, C. J., Kaduk, J. A. & Schenk, H.) Ch. 5.1, 524-537 (2019).
40. Liu, W., Pouvreau, M., Stack, A. G., Yang, X. & Clark, A. E. Concentration dependent interfacial chemistry of the $NaOH_{(aq)}$: gibbsite interface. *Phys. Chem. Chem. Phys.* **24**, 20998–21008 (2022).
41. Wang, H.-W. et al. Structure and stability of SnO_2 nanocrystals and surface-bound water species. *J. Am. Chem. Soc.* **135**, 6885–6895 (2013).
42. Zobel, M., Neder, R. B. & Kimber, S. A. Universal solvent restructuring induced by colloidal nanoparticles. *Science* **347**, 292–294 (2015).
43. Chandran, C. V. et al. Alumina: discriminative analysis using 3D correlation of solid-state NMR parameters. *Chem. Soc. Rev.* **48**, 134–156 (2019).
44. Jiang, S. & ter Horst, J. H. Crystal nucleation rates from probability distributions of induction times. *Cryst. Growth Des.* **11**, 256–261 (2010).
45. Brandel, C. & ter Horst, J. H. Measuring induction times and crystal nucleation rates. *Faraday Discuss* **179**, 199–214 (2015).
46. Wang, C. et al. Phosphate adsorption on amorphous aluminum hydroxide-yielded transition aluminas: insights on fundamental

chemistry and making engineering adsorbents. *J. Water Process. Eng.* **53**, 103677 (2023).
47. Mashkovtsev, M. et al. Spectroscopic study of five-coordinated thermal treated alumina formation: FTIR and NMR applying. *Int. J. Mol. Sci.* **24**, 5151 (2023).
48. Kim, H.-I. & Lee, S. K. Probing the transformation paths from aluminum (oxy)hydroxides (boehmite, bayerite, and gibbsite) to metastable alumina: a view from high-resolution ^{27}Al MAS NMR. *Am. Mineral.* **106**, 389–403 (2021).
49. Huestis, P. L., Graham, T. R., Mergelsberg, S. T. & LaVerne, J. A. Identification of radiolytically-active thermal transition phases in boehmite. *Thermochim. Acta* **689**, 178611 (2020).
50. Apps, J., Neil, J. & Jun, C. Thermochemical properties of gibbsite, bayerite, boehmite, diaspore, and the aluminate ion between 0 and 350 °C. (Lawrence Berkeley Lab., CA. Earth Sciences Div.; Nuclear Regulatory Commission, Washington, DC. Div. of Waste Management., 1989).
51. Wesolowski, D. J. Aluminum speciation and equilibria in aqueous solution: I. The solubility of gibbsite in the system Na-K-Cl-OH-$Al(OH)_4$ from 0 to 100 °C. *Geochim. Cosmochim. Acta* **56**, 1065–1091 (1992).
52. Frydman, L. & Harwood, J. S. Isotropic spectra of half-integer quadrupolar spins from bidimensional magic-angle spinning NMR. *J. Am. Chem. Soc.* **117**, 5367–5368 (2002).
53. Hu, J. Z. et al. Transitions in Al coordination during gibbsite crystallization using high-field ^{27}Al and ^{23}Na MAS NMR spectroscopy. *J. Phys. Chem. C* **121**, 27555–27562 (2017).
54. Loh, J. S. C., Watling, H. R. & Parkinson, G. M. The effect of isotopic substitution of deuterium for hydrogen on the morphology of products precipitated from synthetic Bayer solutions. *J. Cryst. Growth* **237-239**, 2178–2182 (2002).
55. Hawthorne, F. C. & Schindler, M. Understanding the weakly bonded constituents in oxysalt minerals. *Z. Kristallogr. Cryst. Mater.* **223**, 41–68 (2008).
56. Richardson, J. J. et al. Innovation in layer-by-layer assembly. *Chem. Rev.* **116**, 14828–14867 (2016).
57. Bénézeth, P., Hilic, S. & Palmer, D. A. The Solubilities of Gibbsite and Bayerite Below 100 °C in near neutral to basic solutions. *J. Solut. Chem.* **45**, 1288–1302 (2016).
58. Ho, T. A., Greathouse, J. A., Wang, Y. & Criscenti, L. J. Atomistic structure of mineral nano-aggregates from simulated compaction and dewatering. *Sci. Rep.* **7**, 15286 (2017).
59. Nakouzi, E. et al. Impact of solution chemistry and particle anisotropy on the collective dynamics of oriented aggregation. *ACS Nano* **12**, 10114–10122 (2018).
60. Ho, T. A., Rosso, K. M. & Criscenti, L. J. Atomistic mismatch defines energy-structure relationships during oriented attachment of nanoparticles. *J. Phys. Chem. Lett.* **13**, 9339–9347 (2022).
61. Vu, T. V., Ho, T. A. & Criscenti, L. J. Roles of hydrogen bonds and alignment in oriented attachment of gibbsite nanoparticles: insights from molecular dynamics. *J. Phys. Chem. C* (2023).
62. Legg, B. A. & De Yoreo, J. J. Effects of size and shape on the tolerances for misalignment and probabilities for successful oriented attachment of nanoparticles. *Langmuir* **39**, 2985–2994 (2023).
63. Liu, L. et al. Predicting outcomes of nanoparticle attachment by connecting atomistic, interfacial, particle, and aggregate scales. *ACS Nano* **17**, 15556–15567 (2023).
64. Pouvreau, M. et al. An efficient reactive force field without explicit coordination dependence for studying caustic aluminum chemistry. *J. Phys. Chem. Lett.* **14**, 6743–6748 (2023).
65. Neuefeind, J., Feygenson, M., Carruth, J., Hoffmann, R. & Chipley, K. K. The Nanoscale Ordered Materials Diffractometer NOMAD at the spallation neutron source SNS. *Nucl. Instrum. Methods Phys. Res. B Beam Interact. Mater. At.* **287**, 68–75 (2012).

Acknowledgements

This work was supported by supported by Interfacial Dynamics in Radioactive Environments and Materials (IDREAM; FWP 68932), an Energy Frontier Research Center funded by the U.S. Department of Energy (DOE), Office of Science, Basic Energy Sciences (BES). Neutron science experiments were designed at Oak Ridge National Laboratory (ERKCG08). The research at the NOMAD instrument, Spallation Neutron Source at Oak Ridge National Laboratory, was supported by the Scientific User Facilitates Division, BES, DOE. X-ray diffraction, Raman spectroscopy and NMR spectroscopy were performed using resources at the Environmental Molecular Sciences Laboratory (EMSL, grid.436923.9), a DOE Office of Science User Facility sponsored by the Office of Biological and Environmental Research at Pacific Northwest National Laboratory (PNNL). PNNL is a multiprogram national laboratory operated for DOE by Battelle Memorial Institute operating under Contract No. DE AC05-76RL0-1830.

Author contributions

H.-W.W., E.T.N., T.R.G., and M.B. made substantial contributions to the experimental design, acquisition and data analysis. H.-W.W. performed in-situ neutron total scattering and PDF analysis. E.T.N., T.R.G., and M.B. conducted ex-situ characterizations using NMR, Raman, XRD, and SEM measurements. M.P., J.G.R., G.K.S., J.J.D.Y., K.M.R., and C.I.P. discussed the results and edited the manuscript. G.K.S., J.J.D.Y., K.M.R., and C.I.P. also supervised the work. The manuscript was prepared by H.-W.W., E.T.N., and T.R.G. with input from all authors.

Competing interests

The authors declare no competing interests.

Additional information

Supplementary information The online version contains supplementary material available at https://doi.org/10.1038/s42004-024-01285-1.

Correspondence and requests for materials should be addressed to Hsiu-Wen Wang.

Peer review information *Communications Chemistry* thanks David Stephen Wragg and the other, anonymous, reviewer(s) for their contribution to the peer review of this work. A peer review file is available.